



Published in final edited form as:

*Nat Chem Biol.* 2015 October ; 11(10): 807–814. doi:10.1038/nchembio.1908.

## Chemical proteomics reveals a $\gamma$ H2AX-53BP1 interaction in the DNA damage response

Ralph E. Kleiner<sup>1</sup>, Priyanka Verma<sup>1</sup>, Kelly R. Molloy<sup>2</sup>, Brian T. Chait<sup>2</sup>, and Tarun M. Kapoor<sup>1,\*</sup>

<sup>1</sup>Laboratory of Chemistry and Cell Biology, The Rockefeller University, New York, New York 10065

<sup>2</sup>Laboratory of Mass Spectrometry and Gaseous Ion Chemistry, The Rockefeller University, New York, New York 10065

### Abstract

DNA double-strand break repair involves phosphorylation of histone variant H2AX ( $\gamma$ H2AX), which accumulates in foci at sites of damage. In current models, the recruitment of multiple DNA repair proteins to  $\gamma$ H2AX foci depends mainly on recognition of this 'mark' by a single protein, MDC1. However, DNA repair proteins accumulate at  $\gamma$ H2AX sites without MDC1, suggesting that other 'readers' exist. Here, we use a quantitative chemical proteomics approach to profile direct, phospho-selective  $\gamma$ H2AX binders in native proteomes. We identify  $\gamma$ H2AX binders, including the DNA repair mediator, 53BP1, which we show recognizes  $\gamma$ H2AX through its BRCT domains. Furthermore, we investigate targeting of wild-type 53BP1 or a mutant form deficient in  $\gamma$ H2AX binding, to chromosomal breaks resulting from endogenous and exogenous DNA damage. Our results show how direct recognition of  $\gamma$ H2AX modulates protein localization at DNA damage sites, and suggest how specific chromatin 'mark'-'reader' interactions contribute to essential mechanisms ensuring genome stability.

### Introduction

The maintenance of genome stability is a major challenge faced by cells as they are continually exposed to endogenous and exogenous factors that generate DNA damage. Cells have evolved mechanisms to recognize and repair DNA damage, collectively known as the DNA damage response<sup>1</sup>, and defects in this process can lead to disease. In addition, DNA-damaging agents are a mainstay of anti-cancer therapy, and compounds perturbing specific

---

Users may view, print, copy, and download text and data-mine the content in such documents, for the purposes of academic research, subject always to the full Conditions of use:[http://www.nature.com/authors/editorial\\_policies/license.html#terms](http://www.nature.com/authors/editorial_policies/license.html#terms)

\*kapoor@rockefeller.edu.

#### Author Contributions

R. E. K. and T. M. K. conceived the project, designed experiments, and wrote the paper. R. E. K. designed probes, performed mass spectrometry data collection and analysis, performed biochemical characterization, and carried out cellular studies. P. V. validated probes and performed photo-cross-linking experiments. K. R. M. guided mass spectrometry data collection and analysis. B. T. C. directed K. R. M.

#### Competing Financial Interests Statement

The authors declare no competing financial interests.

repair mechanisms are in clinical development<sup>2</sup>. Therefore, characterizing the mechanisms underlying this critical genome surveillance pathway is vital to our understanding of disease etiology and may aid in the development of drugs that target DNA repair.

The cellular response to DNA damage is a tightly controlled process relying on the precise regulation of multiple complex molecular events in the cell. These include the initial detection of DNA damage among a vast excess of undamaged DNA, signal amplification to concentrate DNA damage response factors at DNA lesions, and cell cycle arrest and concomitant DNA repair or apoptosis when the damage is deemed irreparable<sup>1</sup>. The specific orchestration of these events depends on a number of factors, such as the genomic context in which DNA damage occurs, the nature of the damage, and the cell cycle state. Therefore, understanding the molecular basis for the localization of DNA repair factors in response to diverse types of DNA damage and at different stages of repair is critical to gaining a mechanistic understanding of this important cellular process. In eukaryotes, DNA repair occurs within chromatin, which consists of DNA and associated proteins. Chromatin proteins play a central role in the DNA damage response since they facilitate the propagation of cellular signals necessary to recruit DNA repair factors to broken DNA<sup>3</sup>. A focus of much research in the mammalian DNA damage response has been the histone variant H2AX, which is phosphorylated on its C-terminus at DNA double-strand breaks by ATM kinase<sup>4</sup>. Phosphorylated H2AX ( $\gamma$ H2AX) forms megabase-size foci at double-strand breaks and is required for the recruitment of a host of DNA damage response factors, enabling proper repair of DNA damage<sup>1</sup>.

Although it is known that the recruitment of multiple DNA repair factors to  $\gamma$ H2AX foci involves a diverse array of interactions regulated by post-translational modifications, we lack a comprehensive understanding of the contribution of individual 'marks' to protein localization. Current models propose that MDC1 is the major 'reader' of  $\gamma$ H2AX, and affinity pull-downs from nuclear extract with a  $\gamma$ H2AX peptide support this view<sup>5</sup>. The recruitment of downstream repair factors, such as 53BP1, BRCA1, and NBS1, to  $\gamma$ H2AX foci, is considered to rely upon MDC1, as these proteins either directly bind MDC1<sup>6</sup> or recognize MDC1-mediated chromatin 'marks'<sup>7,8</sup>. However, several lines of evidence indicate that DNA repair factors may localize to  $\gamma$ H2AX foci in an MDC1-independent manner. Most importantly, the recruitment of repair factors, such as 53BP1 and NBS1, to  $\gamma$ H2AX sites in MDC1-deficient mouse embryonic fibroblasts (MEFs) is not completely abolished<sup>9</sup>. Additionally, high-resolution microscopy studies of  $\gamma$ H2AX foci composition show that MDC1 does not saturate all available  $\gamma$ H2AX sites and does not overlap with other DNA damage response factors that it is proposed to recruit<sup>10</sup>. Taken together, these data suggest the existence of  $\gamma$ H2AX 'readers' other than MDC1. However, identifying these proteins is challenging as we lack reliable methods to profile  $\gamma$ H2AX-interacting proteins, particularly those that may bind with low affinity (high micromolar  $K_d$ ), as has been reported for numerous protein-protein interactions involving chromatin 'marks'<sup>11</sup>.

Recently, we developed a quantitative chemical proteomics approach, CLASPI (cross-linking-assisted and stable isotope labeling in cell culture-based protein identification) that we used to identify 'readers' of the histone H3 N-terminal tail in cellular lysates<sup>12,13</sup>. In this manuscript, we further develop this methodology to profile direct and phospho-selective

binders of  $\gamma$ H2AX in HeLa cell lysate. In addition to MDC1, we identify ‘readers’ of  $\gamma$ H2AX involved in the DNA damage response, including 53BP1. Since 53BP1 displayed the highest affinity for  $\gamma$ H2AX among the proteins we found, we investigated the significance of this interaction in response to DNA damage. We rationally designed single-point mutations within the 53BP1 tandem BRCT (BRCA1 carboxy-terminal) domains that perturb binding to  $\gamma$ H2AX *in vitro*, and analyzed wild-type and mutant 53BP1 localization and dynamics at  $\gamma$ H2AX foci generated using several different approaches in order to show that a direct interaction between 53BP1 and  $\gamma$ H2AX promotes 53BP1 recruitment to sites of DNA damage in cells.

## Results

### Chemical probes to identify binders of $\gamma$ H2AX

In order to identify  $\gamma$ H2AX ‘readers’ using CLASPI, we needed a probe containing a photo-cross-linker and affinity handle that recapitulates the selectivity and affinity of a known interaction. Guided by available structural and biochemical data<sup>5,14</sup>, we prepared probe C (**1**), which encompasses the C-terminal  $\gamma$ H2AX motif, phospho-SQEY-OH (Fig. 1a and Supplementary Results, Supplementary Fig. 1), necessary and sufficient for binding the tandem BRCT domains of MDC1 (hereafter ‘MDC1-BRCT’). This probe also contained a photo-cross-linker, benzoylphenylalanine, (Fig. 1a and 1b) two residues upstream of the  $\gamma$ H2AX motif, and propargylglycine at the N-terminus for ‘click chemistry’ with azido-diazobenzene-biotin<sup>15</sup>(Fig. 1a). Although this design was effective for identifying histone H3 ‘readers’<sup>12</sup>, when we photo-cross-linked probe C in cellular lysate, we observed a high level of reactivity that was independent of UV treatment but dependent on Cu(I) (Supplementary Fig. 1), suggesting direct protein labeling by azido-diazobenzene-biotin under the particular conditions used. To circumvent this issue, we conjugated azido-diazobenzene-biotin directly to probe C to generate probe 1 (**2**) (Fig. 1a), which obviated the need for performing ‘click chemistry’ in lysate.

We next assayed photo-cross-linking between probe 1 and purified, recombinant MDC1-BRCT. We observed a sigmoidal dose-dependent increase in cross-linking upon increasing the concentration of probe 1 ( $EC_{50} = 0.31 \pm 0.14 \mu\text{M}$ ) (Fig. 1c and Supplementary Fig. 2). In contrast, photo-cross-linking to probe 2 (**3**) (Fig. 1a), containing serine instead of phosphoserine but otherwise identical, proceeded with much lower efficiency (Fig. 1c and Supplementary Fig. 2). Additionally, a 10mer  $\gamma$ H2AX peptide ( $IC_{50} = 4.4 \pm 1.6 \mu\text{M}$ ), but not the analogous non-phosphorylated H2AX peptide ( $IC_{50} > 300 \mu\text{M}$ ), competitively inhibited photo-cross-linking between MDC1-BRCT and probe 1 (Fig. 1d, 1e and Supplementary Fig. 2). Taken together, these results show that our CLASPI probes recapitulate the phospho-selectivity and affinity of a known  $\gamma$ H2AX reader.

### Characterization of $\gamma$ H2AX binders in HeLa cell lysate

After validation with purified, recombinant MDC1-BRCT, we applied our CLASPI probes to identify  $\gamma$ H2AX readers in cellular lysate. We investigated  $\gamma$ H2AX interactions in lysate generated from nocodazole-arrested HeLa cells, since prolonged mitotic arrest is known to induce a DNA damage response<sup>16</sup>. In addition,  $\gamma$ H2AX foci generated during anti-mitotic

drug treatment has been associated with these compounds' efficacy and the DNA damage response in this context is less well understood than in interphase cells.

To profile cellular  $\gamma$ H2AX 'readers', we set up a comparative proteomics experiment consisting of two photo-cross-linking reactions. In the 'affinity filter' experiment (Fig. 2a), isotopically labeled lysate was subjected to UV radiation with probe 1 (5  $\mu$ M) alone or probe 1 (5  $\mu$ M) supplemented with  $\gamma$ H2AX peptide (50  $\mu$ M), which competitively inhibits photo-cross-linking to proteins that bind the peptide in this concentration regime. After UV, reactions were combined, covalent probe-protein complexes were purified with streptavidin, and LC-MS/MS analysis identified captured proteins and quantified the relative amount of photo-cross-linking between the two samples (Fig. 2a). The probes and SILAC labels were switched (termed 'forward' and 'reverse' experiments) to account for differences in protein abundance between the two isotopically labeled lysates.

Our analysis of the 'forward' and 'reverse' 'affinity filter' experiments revealed two proteins (top right quadrant, Fig. 2b) whose photo-cross-linking was inhibited by  $\gamma$ H2AX peptide (50  $\mu$ M): MDC1, the known  $\gamma$ H2AX reader, which exhibited an enrichment ratio (mean of 'forward' and 1/'reverse' SILAC ratios) of 5.3 (Fig. 2c and Supplementary Table 1), and 53BP1 (Supplementary Fig. 3 and Supplementary Table 1), a DNA damage response mediator<sup>17–20</sup>, which showed an enrichment ratio of 2.3. We were unable to detect MCPH1, a reported reader of  $\gamma$ H2AX<sup>21</sup>, using our approach. However, since we have also been unable to detect this protein in whole cell lysate, we suspect that MCPH1 may pose challenges for mass spectrometry analysis. To validate the interaction with 53BP1, we used Western blot to detect 53BP1 after capture with probe 1 (5  $\mu$ M) in lysate from nocodazole-arrested or asynchronous cells and found that, consistent with the mass spectrometry data, protein recovery was inhibited by the  $\gamma$ H2AX peptide (50  $\mu$ M) (Fig. 2d).

To further profile  $\gamma$ H2AX 'readers' in lysate, we undertook a second comparative proteomics experiment assaying phospho-selective interactions. In the 'selectivity filter' experiment, (Fig. 3a), we examined photo-cross-linking between probe 1 and probe 2 (5  $\mu$ M) in lysate. Our analysis identified several proteins (Fig. 3b, top right quadrant) that exhibited phospho-selective reaction with probe 1. Among these proteins, we identified the known  $\gamma$ H2AX reader, MDC1 (enrichment ratio=3.9), as well as 53BP1 (enrichment ratio=4.9), thereby confirming MDC1 selectivity<sup>5</sup> and validating 53BP1 as a selective reader of the phospho-'mark' (Fig. 3b and Supplementary Table 2). We also found HSCARG, HADH2, DHRS4, SORD, UQCC, and PSMB6, which all exhibited reproducible (i.e. variability of 'forward' and 'reverse' ratios < 25% from the mean) enrichment ratios larger than that of MDC1 (Fig. 3b and Supplementary Table 2). Furthermore, we were able to detect several known chromatin-binding proteins— POLG, SIRT1, and MCM2, which all showed reproducible enrichment ratios between 2.5–3.5 (Fig. 3b and Supplementary Table 2). To validate the phospho-selective interactions between  $\gamma$ H2AX and these proteins, we chose two hits that are associated with the DNA damage response, but for which direct molecular mechanisms of recruitment to damaged chromatin are unknown – SIRT1 and HSCARG (Fig. 3c and Supplementary Fig. 3)<sup>22–24</sup>. We transiently expressed GFP-tagged full-length SIRT1 (hereafter 'GFP-SIRT1') or HSCARG (hereafter 'GFP-HSCARG') in HEK 293T cells, and performed photo-cross-linking with probe 1 or probe 2 (5  $\mu$ M) in

lysate harvested from these cells. Western blot demonstrated greater amounts of cross-linking between GFP-SIRT1 and probe 1 compared to probe 2 (Fig. 3d). Similarly, we observed higher efficiency photo-cross-linking between GFP-HSCARG and probe 1 compared to probe 2 (Fig. 3e).

Taken together, our results demonstrate that our approach can identify known direct binders of  $\gamma$ H2AX, such as MDC1, and also suggest the existence of additional ‘readers’, including 53BP1, SIRT1 and HSCARG. Of these proteins, only MDC1 and 53BP1 were identified in both the affinity and selectivity analyses. The inability of 50  $\mu$ M  $\gamma$ H2AX peptide to compete cross-linking to SIRT1 and HSCARG in the ‘affinity filter’ experiment suggests that these proteins do not bind the  $\gamma$ H2AX peptide at this concentration, and therefore are likely to be weak but selective readers of  $\gamma$ H2AX.

### 53BP1 binds $\gamma$ H2AX through its tandem BRCT domains

We next focused on characterizing the interaction between  $\gamma$ H2AX and 53BP1, a protein that promotes non-homologous end joining (NHEJ)-mediated double-strand break repair<sup>25–27</sup>. While 53BP1 co-localizes with  $\gamma$ H2AX foci during the DNA damage response, its recruitment to double-strand breaks relies upon recognition of orthogonal chromatin ‘marks’ – methylated H3 K79<sup>28</sup>, dimethylated H4 K20<sup>29</sup> and ubiquitinated H2A/X K15<sup>30</sup>. We first mapped the region in 53BP1 responsible for  $\gamma$ H2AX binding. Since 53BP1 contains C-terminal tandem BRCT domains (residues 1702-1972), a known phospho-peptide binding motif<sup>31,32</sup>, we investigated this region, as well as residues 956-1354, which have been reported to bind a  $\gamma$ H2AX peptide<sup>33</sup> (Fig. 4a). We generated recombinant GST-fusion proteins containing these regions and assayed photo-cross-linking with probe 1 or probe 2 (5  $\mu$ M), as well as probe 1 (5  $\mu$ M) with  $\gamma$ H2AX competitor peptide (100  $\mu$ M). We observed inefficient and non-phospho-selective photo-cross-linking between residues 956-1354 and our probes (Fig. 4b). In contrast, the BRCT domains fragment displayed robust cross-linking to probe 1 while cross-linking to probe 2 was inefficient (Fig. 4b); in addition, photo-cross-linking to probe 1 was inhibited by the  $\gamma$ H2AX peptide (100  $\mu$ M) (Fig. 4b). These results indicate that the tandem BRCT domains, and not residues 956-1354, mediate phospho-specific binding of 53BP1 to  $\gamma$ H2AX with  $K_d < 100 \mu$ M.

We next measured the affinity of the 53BP1 tandem BRCT domains (hereafter ‘53BP1-BRCT’) for  $\gamma$ H2AX using fluorescence anisotropy. We synthesized fluorescently labeled  $\gamma$ H2AX and H2AX peptides and quantified direct binding to untagged, recombinant 53BP1-BRCT. We found that 53BP1-BRCT bound to fluorescein-phospho-SQEY-OH ( $K_d = 2.7 \pm 0.28 \mu$ M) whereas we could observe only ~10% of bound fluorescein-SQEY-OH peptide by 53BP1-BRCT (50  $\mu$ M) (Fig. 4c). Additionally, we measured the affinity of unlabeled phospho-SQEY-OH tetrapeptide ( $K_i = 7.5 \pm 1.1 \mu$ M) for 53BP1-BRCT using a competition-binding assay (Fig. 4d). Further, we found that 53BP1-BRCT specifically binds the  $\gamma$ H2AX-derived peptide over other phospho-peptides matching the consensus binding motif for tandem BRCT domains<sup>31,32</sup> (phospho-SPTF-OH:  $K_i = 46 \pm 4.4 \mu$ M; phospho-SQEY-NH2:  $K_i = 25 \pm 0.58 \mu$ M) (Fig. 4d). Taken together, our results demonstrate a specific interaction between 53BP1-BRCT and  $\gamma$ H2AX, with comparable affinity to other chromatin-binding interactions<sup>11</sup>.

### 53BP1 Point Mutants with Reduced $\gamma$ H2AX Binding

For functional studies, we needed to generate 53BP1 mutants lacking  $\gamma$ H2AX binding. Therefore, we compared the x-ray crystal structure of 53BP1-BRCT<sup>34</sup> with those of structurally characterized tandem BRCT domains found in MDC1<sup>5</sup> and BRCA1<sup>35</sup> to generate a model for the 53BP1-BRCT and  $\gamma$ H2AX complex. We found two residues (R1811 and K1814 in 53BP1) conserved between all three proteins that were positioned to interact with  $\gamma$ H2AX (Fig. 4e and Supplementary Fig. 4). Therefore, to investigate whether these residues in 53BP1 mediated binding to  $\gamma$ H2AX, we generated recombinant 53BP1-BRCT with either a R1811Q or K1814M mutation and measured affinity of these mutants towards fluorescein-phospho-SQEY-OH. Our results show a 13-fold or > 26-fold decrease in affinity resulting from the R1811Q ( $K_d = 35 \pm 6.2 \mu\text{M}$ ) or K1814M ( $K_d > 70 \mu\text{M}$ ) mutations, respectively (Fig. 4f).

We further characterized the K1814M mutation by introducing GFP-tagged full-length 53BP1 (hereafter 'WT GFP-53BP1') or full-length 53BP1 containing the K1814M mutation (hereafter 'K1814M GFP-53BP1') (Supplementary Fig. 4) into 53BP1<sup>-/-</sup>TRF2<sup>F/-</sup> MEFs and photo-cross-linking with probe 1. Consistent with our earlier findings, reaction with probe 1 was reduced by the  $\gamma$ H2AX competitor peptide and further reduced by the K1814M mutation (Supplementary Fig. 4). These results show that the K1814M mutation can be used to perturb  $\gamma$ H2AX binding in cells.

### Dynamics of 53BP1 recruitment to DNA damage sites

To examine the functional relevance of the  $\gamma$ H2AX-53BP1 interaction in cells, we used quantitative immunofluorescence microscopy and/or live-cell imaging to analyze the localization of WT or K1814M GFP-53BP1 in response to DNA damage using three different assays reporting on endogenous (i.e. telomere deprotection) and exogenous DNA damage (i.e. 'laser scissors' and gamma irradiation). We first studied the role of  $\gamma$ H2AX binding in 53BP1 recruitment to DNA damage sites using 'laser scissors', which enables the real-time observation of protein accumulation at laser-induced DNA breaks in live cells. Briefly, we generated localized DNA damage in a defined nuclear volume, and followed GFP-53BP1 localization to this region by confocal microscopy. We observed the emergence of a 'stripe' of GFP-53BP1 coinciding with the laser-damaged region starting 1–2 min after laser exposure (Fig. 5a and Supplementary Fig. 5) and increasing over the next 6–8 min, at which point the amount of GFP-53BP1 detected within the region remained constant for the duration of the experiment (Fig. 5a and Supplementary Fig. 5).

While we observed substantial variation in the amount of 53BP1 localization to laser 'stripes', possibly due to variation in cell cycle stage, we generally observed larger amounts of WT GFP-53BP1 recruitment compared to K1814M GFP-53BP1. To quantify these differences, we measured average GFP-53BP1 fluorescence intensity in the laser-damaged region during the first 10 min following laser exposure. At 10 min after laser damage, when GFP-53BP1 accumulation had reached a maximum, we found that cells expressing WT protein exhibited 1.7-fold greater median 53BP1 recruitment to the laser 'stripes' than cells expressing K1814M GFP-53BP1 (Supplementary Fig. 5). In addition, we calculated the initial rate of 53BP1 localization by fitting the change in fluorescence in the first 4 min of



increasing GFP-53BP1 signal by linear regression. This analysis revealed that the initial rate of WT-GFP-53BP1 recruitment was 1.7-fold larger compared to K1814M GFP-53BP1 (Fig. 5b). Taken together, our results show that  $\gamma$ H2AX binding by the 53BP1 tandem BRCT domains increases the kinetics and overall amount of 53BP1 recruitment to DNA damage produced by ‘laser scissors’.

### 53BP1 recruitment to DNA damage in the absence of MDC1

We also analyzed localization of WT and K1814M GFP-53BP1 to DNA damage sites in MDC1<sup>-/-</sup> MEFs (Supplementary Fig. 4). MDC1 mediates 53BP1 foci formation by promoting chromatin ubiquitination<sup>36,37</sup> and methylation<sup>8</sup>, but is not required for its initial recruitment<sup>9</sup>. In cells expressing WT GFP-53BP1, but lacking MDC1, the kinetics and total accumulation of GFP-53BP1 in the first 10 minutes after laser irradiation were significantly attenuated compared to cells with MDC1 (Fig. 5c and Supplementary Fig. 5), however we still observed DNA-damage-induced protein localization in most cells. In contrast, in MDC1<sup>-/-</sup> MEFs expressing K1814M GFP-53BP1, we did not observe redistribution of 53BP1 upon laser damage in the majority of cells. We quantified these differences by calculating the median rate and amount of WT and K1814M GFP-53BP1 recruitment (Fig. 5d and Supplementary Fig. 5) and found these values to be 4.4-fold greater and 3.5-fold greater, respectively, in cells containing WT GFP-53BP1. These results show that in the absence of MDC1, 53BP1 recruitment to DNA damage sites depends on a direct interaction with  $\gamma$ H2AX.

### 53BP1 localization at telomeric DNA damage foci

We next analyzed 53BP1 localization in response to endogenous DNA damage produced by conditional deletion of TRF2, a subunit of the ‘shelterin’ complex<sup>26</sup>. TRF2 depletion initiates an ATM-mediated DNA damage response producing  $\gamma$ H2AX foci at telomeres<sup>26</sup>. In WT and K1814M GFP-53BP1 cells, we observed a maximal response, as determined by the number and intensity of  $\gamma$ H2AX and 53BP1 foci, 72 hr after TRF2 deletion (Fig. 6a). We more frequently observed  $\gamma$ H2AX foci lacking corresponding 53BP1 foci in the mutant cell line. To quantify these differences, we measured two parameters: first, the ratio of 53BP1/ $\gamma$ H2AX intensity evaluated over ~7000 foci per condition, and second, the number of foci per cell, as correlated with the extent of repair<sup>38</sup>. We found the median 53BP1/ $\gamma$ H2AX intensity to be 1.4-fold greater in WT cells compared to K1814M cells (WT ratio=0.72, n=7329 foci; K1814M ratio=0.52, n=6985 foci) (Fig. 6b and Supplementary Fig. 6), indicating greater accumulation of WT protein at  $\gamma$ H2AX foci. We also observed a 2-fold increase in the amount of  $\gamma$ H2AX foci defective in 53BP1 localization (53BP1/ $\gamma$ H2AX ratio < 0.125) present in mutant 53BP1 cells (1269/6985 foci, 18%) as compared to in WT 53BP1 cells (647/7329 foci, 8.8%) (Fig. 6b and Supplementary Fig. 6). Additionally, mutant 53BP1 cells displayed on average 26% more  $\gamma$ H2AX foci per cell (WT=27  $\pm$  2.3  $\gamma$ H2AX foci/cell; K1814M=34  $\pm$  7.6  $\gamma$ H2AX foci/cell) (Supplementary Fig. 6), consistent with a repair defect. Taken together, these results show that the K1814M mutation that reduces  $\gamma$ H2AX binding results in measurable defects in 53BP1 localization at telomeric  $\gamma$ H2AX foci.

### 53BP1 localization at IR-induced DNA damage foci

We further characterized 53BP1 recruitment to DNA damage by treating cells with ionizing radiation (IR), a standard assay for the analysis of double-strand breaks. We monitored  $\gamma$ H2AX and 53BP1 foci at 3 time points after subjecting cells to 2 different doses of IR, 1 Gy or 12 Gy. Consistent with literature reports, 1 Gy IR resulted in  $\sim$ 30  $\gamma$ H2AX foci per cell within minutes (Supplementary Fig. 7). These foci gradually disappeared over the course of several hours and  $>$  70% were resolved by 24 hr after IR exposure (Supplementary Fig. 7). We analyzed  $\gamma$ H2AX and 53BP1 foci at early (15 min after 1 Gy) and intermediate (4 hr after 1 Gy) time points after IR, but did not observe significant differences in the distribution of 53BP1/ $\gamma$ H2AX intensity between WT and K1814M proteins (Supplementary Fig. 7). In contrast, analysis of foci detected 24 hr after DNA damage revealed significant differences. In K1814M cells, the median 53BP1/ $\gamma$ H2AX intensity was reduced (WT = 0.89, n = 1295 foci; K1814M = 0.57, n = 1074 foci) (Supplementary Fig. 7) and 1.6-fold more foci exhibited defective (i.e. ratio  $<$  0.25) 53BP1 localization (WT: 62/1295 foci, 20%; K1814M: 334/1074 foci, 31%) (Supplementary Fig. 7).

As expected, 12 Gy IR produced more  $\gamma$ H2AX foci per cell than 1 Gy IR (Supplementary Fig. 8). Similar to the results after 1 Gy IR, quantification of 53BP1/ $\gamma$ H2AX intensity at 24 hr after 12 Gy IR (Fig. 6c and 6d) revealed substantial differences in 53BP1 accumulation, whereas analysis at early (2 hr) and intermediate (8 hr) (Fig. 6d and Supplementary Fig. 8) stages of repair did not. At 24 hr, we found that the median 53BP1/ $\gamma$ H2AX ratio in WT 53BP1 cells (WT = 0.89, n = 3917 foci) was 1.7-fold greater than in mutant cells (K1814M = 0.53, n = 4768 foci) (Fig. 6d) and that 1.6-fold more  $\gamma$ H2AX foci in mutant cells exhibited defective 53BP1 localization (i.e. ratio  $<$  0.25) (WT: 786/3917 foci, 20%; K1814M: 1456/4768 foci, 31%) (Supplementary Fig. 8).

In addition to global differences in 53BP1 accumulation at late stage  $\gamma$ H2AX foci, we also observed a striking phenotype in a subset of cells (15%) expressing mutant 53BP1 analyzed 24 hr after 12 Gy IR (Fig. 6c and 6e). These cells contained  $\sim$ 10–20  $\gamma$ H2AX foci (similar to the population average) but no corresponding 53BP1 foci. Instead, 53BP1 staining was diffuse, but still localized to the nucleus (Fig. 6c see inset). In cells with WT GFP-53BP1, only 3% showed this gross defect in 53BP1 co-localization (Fig. 6c and Fig. 6e). This population may reflect a particular cell cycle state, although we note that interpreting and dissecting this phenotype may be challenging in this experimental settings, as these experiments were performed in SV40LT-immortalized MEFs, which are defective in multiple cell-cycle checkpoints<sup>39</sup>. Taken together, our findings indicate that proper targeting of 53BP1 to late-repairing DNA damage foci involves an interaction mediated by 53BP1's BRCT domains. Such foci are likely to be enriched in heterochromatin relative to the foci analyzed at earlier time points<sup>40</sup>.

### Discussion

In this study, we used a quantitative chemical proteomics approach to identify 53BP1, SIRT1, and HSCARG, in addition to MDC1, as 'readers' of  $\gamma$ H2AX – a DNA-damage associated chromatin 'mark'. We focused on direct 53BP1 recognition of  $\gamma$ H2AX and showed that disrupting this interaction leads to differences in accumulation rate, MDC1-



independent recruitment, and 53BP1 retention at DNA breaks. Our work demonstrates how phosphorylation of H2AX mediates diverse phospho-protein interactions involved in the DNA damage response.

Many of the key players in the DNA damage response are widely conserved among eukaryotes. Notably, yeast possess homologs of 53BP1– the DNA repair factors Rad9 and Crb2. These proteins bind to phosphorylated H2A ( $\gamma$ H2A') using tandem BRCT domains<sup>41–43</sup>, which are structurally conserved in 53BP1 homologs from yeast to human (Supplementary Fig. 9). However, these domains are not considered functionally significant in mammalian 53BP1, as studies with constructs lacking them have not revealed defects in DNA repair or recruitment to  $\gamma$ H2AX foci<sup>44–46</sup>. This raises the question: what is the role of the tandem BRCT domains in 53BP1 that has necessitated their evolutionary conservation? Our work provides a resolution to this question by showing that  $\gamma$ H2A/ $\gamma$ H2AX recognition through tandem BRCT domains is a conserved feature of 53BP1 homologs from yeast to man. The key difference is that the role of this interaction has diverged. Our findings suggest that rather than serving as a necessary step for of 53BP1 recruitment to DNA damage sites, as in yeast, the mammalian 53BP1- $\gamma$ H2AX interaction has acquired a specialized function– contributing to 53BP1 recruitment kinetics, accumulation during late-stage DNA repair, and localization to telomeres. Interestingly, DNA damage signaling in mammals, including the recruitment of 53BP1 and BRCA1, relies upon chromatin ubiquitination by RNF8 and RNF168, whose homologs have not been detected in yeast<sup>30</sup>. We speculate that the increased dependence on ubiquitin-‘marks’ for DNA repair factor recruitment in mammals has enabled the reassignment of phospho-‘mark’-mediated interactions to other functions in the DNA damage response.

Together with published reports, our findings demonstrate that accumulation of 53BP1 at double-strand breaks involves 3 possible chromatin-mediated interactions. How do these binding events facilitate 53BP1 recruitment to DNA damage sites? Recognition of methylated H4 K20 by 53BP1's tandem Tudor domains is a low-affinity interaction ( $K_d \sim 20 \mu\text{M}$ )<sup>29</sup> and binding of ubiquitinated H2A K15 by the UDR motif could not be readily detected using biophysical methods and is also likely to be a weak interaction<sup>30</sup>. Therefore, we favor a model in which 53BP1 localization relies upon multiple interactions and wherein no single epitope provides sufficient binding energy for stable association (Supplementary Fig. 9). This binding mode provides multiple points of regulation that enable the precise control of 53BP1 activity in response to diverse cellular parameters such as chromatin architecture and cell cycle stage. While recognition of methyl and ubiquitin ‘marks’<sup>30</sup> is responsible for the majority of 53BP1 recruitment to DNA damage sites, a direct interaction with  $\gamma$ H2AX is involved in specific contexts, such as at late-repairing foci and telomeric sites. Interestingly, these late-repairing  $\gamma$ H2AX foci may occur primarily in heterochromatic regions, where DNA repair is known to proceed more slowly<sup>47</sup>. And consistent with our findings, the BRCT domains of 53BP1 have been implicated in heterochromatic DNA repair; however, this process was not examined in the context of direct  $\gamma$ H2AX recognition<sup>48</sup>. Similarly, telomeres are proximal to heterochromatic regions<sup>49</sup>. The heterogeneous response observed in individual cells at late time points is also suggestive of cell cycle-regulation of the  $\gamma$ H2AX interaction. Further studies will be needed to dissect the contributions of these various factors to 53BP1-mediated DNA repair. Our studies also point

to recognition of  $\gamma$ H2AX by SIRT1 and HSCARG. Similar to our findings with 53BP1, these binding events may be relevant in particular contexts, or in combination with other interactions.

Recognition of pSer/pThr can be mediated by BRCT domains, conserved protein-interaction motifs frequently found in DNA damage response proteins. Predicting relevant ligands for these domains *a priori* is challenging, and potential phospho-peptide binding by 53BP1-BRCT has been largely ignored. Our findings combined with available structural data suggest a mode of recognition comparable to what has been observed in other mammalian tandem BRCT domains including those in MDC1<sup>5</sup> and BRCA1<sup>14</sup>. Similar to these domains, 53BP1-BRCT binds multiple phospho-peptides matching the pS/T-X-X-F/Y consensus sequence, although the peptides examined in this work were bound with reduced affinity compared to  $\gamma$ H2AX. Nevertheless, since the K1814M mutation examined in this study would likely perturb interactions with other cellular phospho-peptides, we cannot exclude the possibility that the observed cellular effects may result from impairment of 53BP1-BRCT interactions with other phospho-proteins in addition to  $\gamma$ H2AX. To our knowledge, however, no other phosphorylated cellular ligand for 53BP1-BRCT has been reported, and therefore perturbation of  $\gamma$ H2AX recognition remains the only known functional output of the K1814M mutation.

Many characterized chromatin-binding modules exhibit weak monovalent binding when assayed *in vitro*. These interactions are thought to be relevant in a multivalent context, where synergistic binding events between multiple chromatin-binding domains and histone 'marks' can generate interactions with high affinity and specificity<sup>50</sup>. Our work demonstrates the utility of photo-cross-linking-based approaches for profiling direct, modification-dependent protein-protein interactions of varying affinities in lysate, and highlights the importance of these interactions in processes that ensure genome stability. Adapting such approaches to *in vivo* systems will be the next step to enable the characterization of these interactions in their native context.

## Online Methods

### Plasmids

A plasmid encoding cDNA for human MDC1-BRCT<sup>5</sup> was a gift from Stephen Jackson. MDC1-BRCT (residues 1883-2089) was cloned into pDONR201 and then pDEST15 using Gateway technology (Life Technologies). A plasmid encoding cDNA of human 53BP1 was a gift from Titia de Lange (Addgene plasmid #19836)<sup>26</sup>. 53BP1-BRCT (residues 1702-1972) was cloned into pGEX-6P-1 (GE Healthcare) using BamHI and XhoI restriction sites. R1811Q and K1814M mutations were introduced into 53BP1 using overlap extension PCR with mutagenic primers. Human 53BP1 (residues 956-1354) was cloned into pGEX-6P-1 using EcoRI and XhoI restriction sites. Full-length wild-type 53BP1 and K1814M 53BP1 were cloned into pDONR201 and then an amino-terminal GFP-fusion retroviral vector based upon pMSCVpuro using Gateway technology. A plasmid encoding cDNA for human SIRT1 was a gift from Michael Greenberg (Addgene plasmid #1791) and a plasmid encoding cDNA for human HSCARG was a gift from Nicola Burgess-Brown (Addgene plasmid #39016). Full-length SIRT1 and full-length HSCARG were cloned into a

modified pCDNA3.1/Myc-HisA (Life Technologies) vector containing an N-terminal eGFP tag.

### Peptide probe synthesis

$\gamma$ H2AX- and H2AX-peptide probes (probe 1 and probe 2) were prepared by conjugating a biotin-PEG-diazobenzene- $N_3$  affinity tag<sup>15</sup> to alkyne- and benzophenone-containing peptides using Cu(I)-catalyzed Azide-Alkyne Cycloaddition (CuAAC). Benzophenone and alkyne-containing modified peptides (e.g. probe C) were synthesized by automated solid-phase peptide synthesis using standard conditions. The peptide and biotin affinity tag were reacted together in the presence of  $CuSO_4$ , ascorbic acid, and TBTA using standard conditions. Probes were purified by reverse-phase HPLC using a C18 stationary phase and elution with a gradient of water and acetonitrile. MALDI-MS and ESI-MS characterization data are provided in Supplementary Table 1.

### Protein expression and purification

All proteins were expressed in *Escherichia coli* BL21(Rosetta) by induction overnight with IPTG (0.5 mM) at 18 °C. After cell lysis, GST-fusion proteins were captured on a GSTrap 4B (GE Healthcare) affinity matrix and eluted with glutathione-containing buffer (50 mM HEPES pH 7.5, 150 mM NaCl, 10 mM L-glutathione, 1 mM DTT). Proteins were then dialyzed to remove glutathione and concentrated if needed using Amicon Ultra-4 centrifugal filter units (EMD Millipore). For wild-type and mutant 53BP1-BRCT proteins, the GST tag was cleaved by incubation with PreScission protease overnight, and the untagged proteins were purified by anion-exchange chromatography as described previously<sup>34</sup>.

### Photo-cross-linking and streptavidin enrichment

Photo-cross-linking of lysate proteins to probes **1** and **2** was performed as previously described<sup>12</sup>. Following photo-cross-linking, SDS (0.5%) was added to the samples and they were incubated with streptavidin agarose resin (Thermo Scientific) for 90 min at RT. The resin was washed with 1% SDS in PBS (3X), 6M urea and 0.1% SDS in PBS (6X), and 0.1% SDS in 250 mM  $NH_4HCO_3$  (3X). Proteins were eluted by incubating twice with sodium dithionite-containing buffer (25 mM  $Na_2S_2O_4$ , 0.1% SDS, 250 mM  $NH_4HCO_3$ ) for 1 hr at RT. Samples were evaporated to dryness in a SpeedVac. For photo-cross-linking to purified proteins, recombinant protein (200 nM) was incubated with probe 1 or probe 2 for 20 min on ice and then irradiated at 365 nm using a Spectroline ML-3500S UV lamp for 15 min on ice.

### Preparation of whole-cell lysates

Whole-cell lysate from nocodazole-arrested or asynchronous HeLa S3 cells was prepared as previously described using a cryogenic grinding-based protocol<sup>12</sup>. For proteomic analysis, HeLa S3 cells were cultured in medium containing  $^{13}C_6^{15}N_4$ -L-arginine (22 mg/L) and  $^{13}C_6^{15}N_2$ -L-lysine (50 mg/L) or L-arginine (21 mg/L) and L-lysine (48 mg/L).

## Mass spectrometry

Mass spectrometry was performed essentially as described previously<sup>12</sup>. Dried protein samples were resuspended in LDS sample buffer (Life Technologies), reduced and alkylated, and separated on a 4–12% Bis-Tris gradient gel (Life Technologies), followed by in-gel trypsin digestion. Tryptic peptides were purified and analyzed on an LTQ-Orbitrap XL mass spectrometer (Thermo Scientific). Protein identification and quantitation of SILAC peptide ratios was performed using MaxQuant<sup>51</sup> version 1.2.2.5.

## Fluorescence anisotropy

NH<sub>2</sub>-phospho-SQEY-OH or NH<sub>2</sub>-SQEY-OH peptides were prepared by automated solid-phase peptide synthesis by standard methods and reacted with NHS-fluorescein (Thermo Scientific). Fluorescein-labeled tetrapeptides were purified by reverse-phase HPLC. Binding assays with 53BP1-BRCT constructs were performed by combining fluorescein-labeled peptide (50 nM) with varying concentrations of purified protein in buffer (50 mM HEPES pH 7.5, 150 mM NaCl, 1 mM DTT). After equilibration, fluorescence anisotropy was measured using a BioTek Synergy Neo microplate reader. Dissociation constants ( $K_d$ ) were calculated by fitting measured values to a four-parameter sigmoidal dose-response curve. For competition binding assays, fluorescein-phospho-SQEY peptide (50 nM) was combined with 53BP1-BRCT (6  $\mu$ M) and varying concentrations of competitor peptide in buffer (50 mM HEPES pH 7.5, 150 mM NaCl, 1 mM DTT) and fluorescence anisotropy was measured as above. The half maximal inhibitory concentration ( $IC_{50}$ ) was calculated by fitting measured values to a four-parameter sigmoidal dose-response curve. Inhibition constants ( $K_i$ ) were derived from  $IC_{50}$  using the following equation:

$$K_i = B \cdot I \cdot K_d / (L_T \cdot R_T) + B \cdot (-R_T - L_T + B - K_d)$$

B = bound ligand concentration; I = inhibitor concentration;  $L_T$  = total ligand concentration;  $R_T$  = total receptor concentration.

## Cell culture and retroviral transduction

MDC1<sup>-/-26</sup> and TRF2<sup>-F53BP1-/-</sup> MEFs<sup>26</sup> were described previously. Cells were cultured at 37 °C in a humidified atmosphere with 5% CO<sub>2</sub> in DMEM (Life Technologies) supplemented with 15% FBS (HyClone) (for MEFs) or 10% BCS (HyClone) (for Phoenix cells), 1X penicillin-streptomycin and non-essential amino acids (Life Technologies) and 2 mM L-glutamine (Life Technologies). To generate retrovirus, Phoenix cells were transfected using a calcium phosphate protocol. Medium containing retrovirus was harvested, supplemented with 4  $\mu$ g/mL Polybrene (Sigma), and applied to MEFs followed by selection with puromycin (Sigma).

## Immunofluorescence microscopy

Telomeric foci were generated by TRF2 deletion in TRF2<sup>F/-</sup> 53BP1<sup>-/-</sup> Rosa26 Cre-ER<sup>T1</sup> MEFs by treating with 4-HT (Sigma) as described previously<sup>27</sup>. Genomic foci were generated by subjecting cells to gamma rays from a Cs-137 source. For imaging  $\gamma$ H2AX and GFP-53BP1 foci, cells on coverslips were fixed for 10 min at RT in PBS containing 3%

paraformaldehyde and 2% sucrose adjusted to pH 7.3. After fixation, cells were blocked and permeabilized with PBS containing 0.1% Triton X-100, 0.1% BSA (Sigma), and 3% donkey serum (Sigma). The following primary antibodies were used: anti-phospho-Histone H2A.X clone JBW301 (EMD Millipore #05-636-I, used at 1:1000); anti-GFP (raised against full-length GFP and affinity purified, used at 1 µg/mL). Secondary antibodies raised in donkey (Jackson Immunoresearch) were used at 2 µg/mL and DNA was stained with Hoechst 33342 (Thermo Scientific, 1 µg/mL). Coverslips were mounted in ProLong Gold AntiFade Reagent (Life Technologies) and sealed with nail polish. Images of fixed cells were acquired using Metamorph software and a Zeiss Axiovert 200M microscope equipped with 63X objective and EMCCD camera (Andor iXon). For quantification of GFP-53BP1/γH2AX intensity at foci, fluorescence micrographs were background subtracted using a rolling ball with 3 pixel radius (ImageJ) and γH2AX foci > 4 pixels in area were defined using a particle identification algorithm (ImageJ). GFP-53BP1 and γH2AX integrated fluorescence intensity were measured in the defined focal region.

### Western blot

For Western blot analysis, the following antibodies were used: anti-53BP1 (Bethyl, #A300-272A, used at 1:1000), anti-GFP (used at 1 µg/mL), anti-α-tubulin clone DM1α, (Sigma #T6199, used at 1:5000). IRDye-conjugated secondary antibodies raised in goat and IRDye-conjugated streptavidin were purchased from LI-COR Biosciences and used according to the manufacturer's instructions.

### Live cell imaging

For live-cell imaging, cells grown on glass-bottom culture dishes (MatTek Corp), were incubated for 10 min with Hoechst 33342 (0.5 µg/mL) in Leibovitz's L-15 medium without phenol red (Life Technologies) supplemented with 15% FBS (HyClone). Cells were maintained at 37 °C and a defined nuclear volume was exposed to a 405 nm laser (50% power output, 1 sec) using the Photonics Instruments Digital Mosaic system (Andor). Confocal GFP fluorescence micrographs were acquired immediately after laser damage using Metamorph software and a Zeiss Axiovert 200 microscope equipped with 63X objective, UltraView spinning disk confocal head (Perkin Elmer), EMCCD camera (Andor iXon) and solid-state 491 nm laser (Spectral Applied). To quantify GFP-53BP1 recruitment, average GFP fluorescence intensity was measured in a 6-pixel-wide region encompassing the site of laser exposure (ImageJ).

### Supplementary Material

Refer to Web version on PubMed Central for supplementary material.

### Acknowledgments

We are grateful to Titia de Lange for the generous gift of 53BP1- and MDC1-deficient MEFs and for helpful discussions. We thank Francisca Lotterberger for advice and assistance with DNA damage assays. Live-cell imaging was performed at the Rockefeller University Bio-Imaging Resource Center. We thank Pablo Ariel for technical assistance with laser scissors. Peptide synthesis was performed by the Rockefeller University Proteomics Resource Center. We thank Rudolf Pisa for assistance with peptide probe synthesis, and Emily Foley for assistance with pilot experiments. R. E. K. is the Miles S. Nadal Fellow of the Damon Runyon Cancer Research Foundation

(DRG-2118-12). The authors acknowledge support from the NIH (GM98579 to T. M. K. and P41 GM103314 and GM109824 to B. T. C).

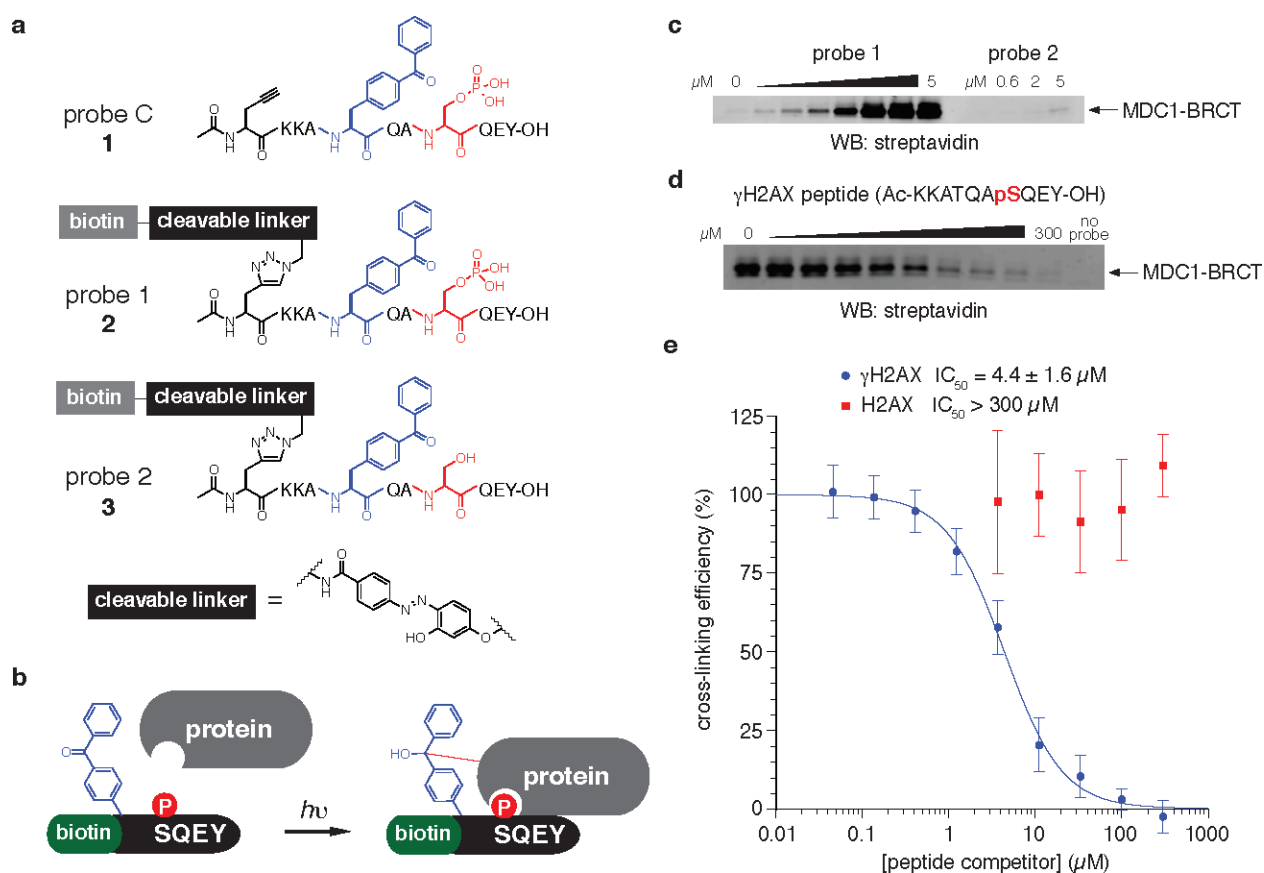
## References

1. Ciccia A, Elledge SJ. The DNA damage response: making it safe to play with knives. *Mol Cell*. 2010; 40:179–204.10.1016/j.molcel.2010.09.019 [PubMed: 20965415]
2. Lord CJ, Ashworth A. The DNA damage response and cancer therapy. *Nature*. 2012; 481:287–294.10.1038/nature10760 [PubMed: 22258607]
3. Jenuwein T, Allis CD. Translating the histone code. *Science*. 2001; 293:1074–1080.10.1126/science.1063127 [PubMed: 11498575]
4. Rogakou EP, Pilch DR, Orr AH, Ivanova VS, Bonner WM. DNA double-stranded breaks induce histone H2AX phosphorylation on serine 139. *J Biol Chem*. 1998; 273:5858–5868. [PubMed: 9488723]
5. Stucki M, et al. MDC1 Directly Binds Phosphorylated Histone H2AX to Regulate Cellular Responses to DNA Double-Strand Breaks. *Cell*. 2005; 123:1213–1226. [PubMed: 16377563]
6. Spycher C, et al. Constitutive phosphorylation of MDC1 physically links the MRE11-RAD50-NBS1 complex to damaged chromatin. *J Cell Biol*. 2008; 181:227–240.10.1083/jcb.200709008 [PubMed: 18411308]
7. Jackson SP, Durocher D. Regulation of DNA damage responses by ubiquitin and SUMO. *Mol Cell*. 2013; 49:795–807.10.1016/j.molcel.2013.01.017 [PubMed: 23416108]
8. Pei H, et al. MMSET regulates histone H4K20 methylation and 53BP1 accumulation at DNA damage sites. *Nature*. 2011; 470:124–128.10.1038/nature09658 [PubMed: 21293379]
9. Lou Z, et al. MDC1 Maintains Genomic Stability by Participating in the Amplification of ATM-Dependent DNA Damage Signals. *Mol Cell*. 2006; 21:187–200. [PubMed: 16427009]
10. Nakamura AJ, Rao VA, Pommier Y, Bonner WM. The complexity of phosphorylated H2AX foci formation and DNA repair assembly at DNA double-strand breaks. *Cell cycle*. 2010; 9:389–397. [PubMed: 20046100]
11. Taverna SD, Li H, Ruthenburg AJ, Allis CD, Patel DJ. How chromatin-binding modules interpret histone modifications: lessons from professional pocket pickers. *Nature structural & molecular biology*. 2007; 14:1025–1040.10.1038/nsmb1338
12. Li X, et al. Quantitative chemical proteomics approach to identify post-translational modification-mediated protein-protein interactions. *J Am Chem Soc*. 2012; 134:1982–1985. [PubMed: 22239320]
13. Li X, et al. Examining post-translational modification-mediated protein-protein interactions using a chemical proteomics approach. *Protein Sci*. 2013; 22:287–295. [PubMed: 23281010]
14. Campbell SJ, Edwards RA, Glover JNM. Comparison of the structures and peptide binding specificities of the BRCT domains of MDC1 and BRCA1. *Structure*. 2010; 18:167–176. [PubMed: 20159462]
15. Yang YY, Grammel M, Raghavan AS, Charron G, Hang HC. Comparative analysis of cleavable azobenzene-based affinity tags for bioorthogonal chemical proteomics. *Chemistry & biology*. 2010; 17:1212–1222.10.1016/j.chembiol.2010.09.012 [PubMed: 21095571]
16. Orth JD, Loewer A, Lahav G, Mitchison TJ. Prolonged mitotic arrest triggers partial activation of apoptosis, resulting in DNA damage and p53 induction. *Molecular biology of the cell*. 2012; 23:567–576.10.1091/mbc.E11-09-0781 [PubMed: 22171325]
17. DiTullio RA Jr, et al. 53BP1 functions in an ATM-dependent checkpoint pathway that is constitutively activated in human cancer. *Nature cell biology*. 2002; 4:998–1002.10.1038/ncb892 [PubMed: 12447382]
18. Fernandez-Capetillo O, et al. DNA damage-induced G2-M checkpoint activation by histone H2AX and 53BP1. *Nature cell biology*. 2002; 4:993–997.10.1038/ncb884 [PubMed: 12447390]
19. Schultz LB, Chehab NH, Malikzay A, Halazonetis TD. p53 binding protein 1 (53BP1) is an early participant in the cellular response to DNA double-strand breaks. *J Cell Biol*. 2000; 151:1381–1390. [PubMed: 11134068]

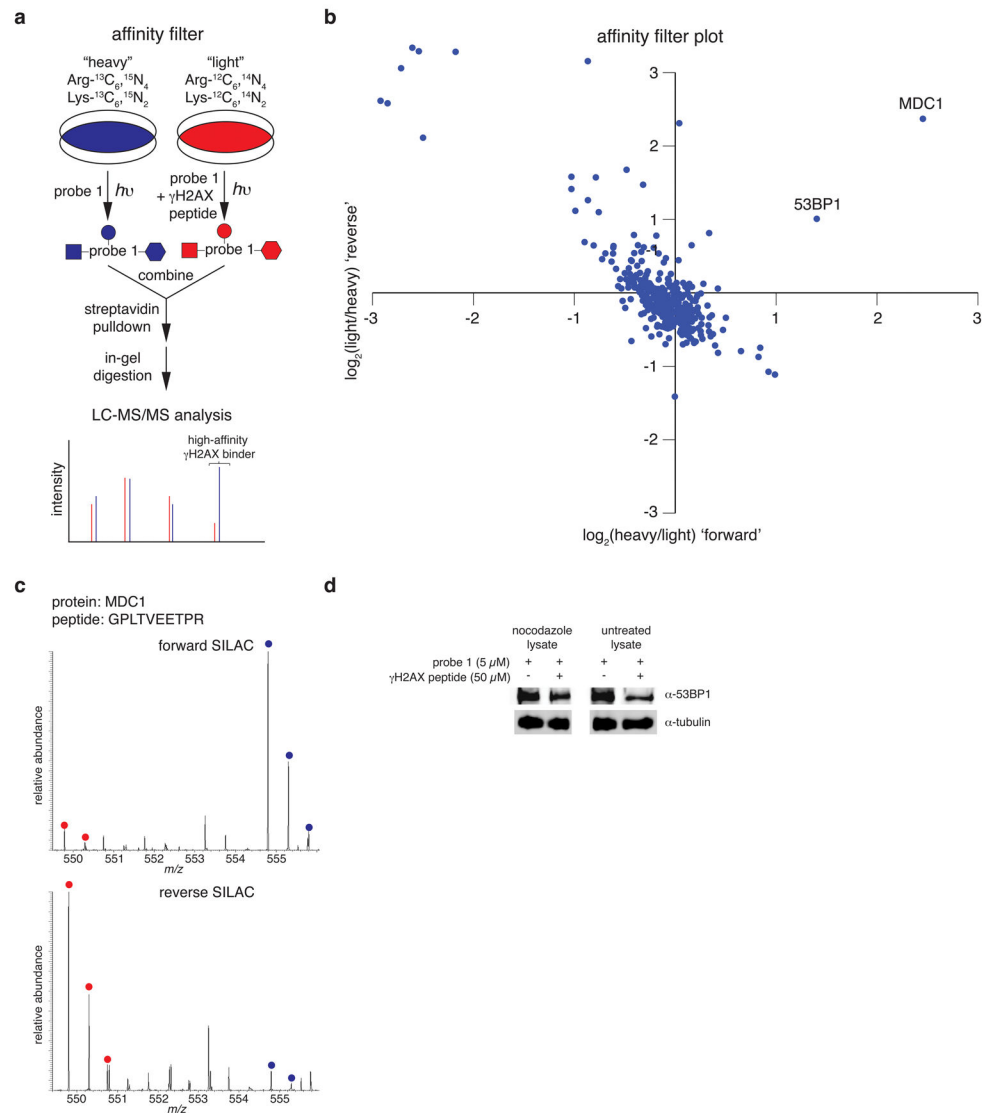


20. Wang B, Matsuoka S, Carpenter PB, Elledge SJ. 53BP1, a mediator of the DNA damage checkpoint. *Science*. 2002; 298:1435–1438.10.1126/science.1076182 [PubMed: 12364621]
21. Wood JL, Singh N, Mer G, Chen J. MCPH1 functions in an H2AX-dependent but MDC1-independent pathway in response to DNA damage. *J Biol Chem*. 2007; 282:35416–35423.10.1074/jbc.M705245200 [PubMed: 17925396]
22. Dobbin MM, et al. SIRT1 collaborates with ATM and HDAC1 to maintain genomic stability in neurons. *Nature neuroscience*. 2013; 16:1008–1015.10.1038/nn.3460 [PubMed: 23852118]
23. Hu B, Li S, Zhang X, Zheng X. HSCARG, a novel regulator of H2A ubiquitination by downregulating PRC1 ubiquitin E3 ligase activity, is essential for cell proliferation. *Nucleic acids research*. 2014; 42:5582–5593.10.1093/nar/gku230 [PubMed: 24711370]
24. Oberdoerffer P, et al. SIRT1 redistribution on chromatin promotes genomic stability but alters gene expression during aging. *Cell*. 2008; 135:907–918.10.1016/j.cell.2008.10.025 [PubMed: 19041753]
25. Bunting SF, et al. 53BP1 inhibits homologous recombination in Brca1-deficient cells by blocking resection of DNA breaks. *Cell*. 2010; 141:243–254.10.1016/j.cell.2010.03.012 [PubMed: 20362325]
26. Dimitrova N, Chen YC, Spector DL, de Lange T. 53BP1 promotes non-homologous end joining of telomeres by increasing chromatin mobility. *Nature*. 2008; 456:524–528.10.1038/nature07433 [PubMed: 18931659]
27. Zimmermann M, Lottersberger F, Buonomo SB, Sfeir A, de Lange T. 53BP1 regulates DSB repair using Rif1 to control 5' end resection. *Science*. 2013; 339:700–704.10.1126/science.1231573 [PubMed: 23306437]
28. Huyen Y, et al. Methylated lysine 79 of histone H3 targets 53BP1 to DNA double-strand breaks. *Nature*. 2004; 432:406–411.10.1038/nature03114 [PubMed: 15525939]
29. Botuyan MV, et al. Structural basis for the methylation state-specific recognition of histone H4-K20 by 53BP1 and Crb2 in DNA repair. *Cell*. 2006; 127:1361–1373.10.1016/j.cell.2006.10.043 [PubMed: 17190600]
30. Fradet-Turcotte A, et al. 53BP1 is a reader of the DNA-damage-induced H2A Lys 15 ubiquitin mark. *Nature*. 2013; 499:50–54. [PubMed: 23760478]
31. Manke IA, Lowery DM, Nguyen A, Yaffe MB. BRCT Repeats as Phosphopeptide-Binding Modules Involved in Protein Targeting. *Science*. 2003; 302:636–639. [PubMed: 14576432]
32. Yu X, Chini CC, He M, Mer G, Chen J. The BRCT Domain Is a Phospho-Protein Binding Domain. *Science*. 2003; 302:639–642. [PubMed: 14576433]
33. Ward IM, Minn K, Jorda KG, Chen J. Accumulation of checkpoint protein 53BP1 at DNA breaks involves its binding to phosphorylated histone H2AX. *J Biol Chem*. 2003; 278:19579–19582.10.1074/jbc.C300117200 [PubMed: 12697768]
34. Joo WS, et al. Structure of the 53BP1 BRCT region bound to p53 and its comparison to the Brca1 BRCT structure. *Genes Dev*. 2002; 16:583–593. [PubMed: 11877378]
35. Clapperton JA, et al. Structure and mechanism of BRCA1 BRCT domain recognition of phosphorylated BACH1 with implications for cancer. *Nature structural & molecular biology*. 2004; 11:512–518.10.1038/nsmb775
36. Huen MS, et al. RNF8 transduces the DNA-damage signal via histone ubiquitylation and checkpoint protein assembly. *Cell*. 2007; 131:901–914.10.1016/j.cell.2007.09.041 [PubMed: 18001825]
37. Kolas NK, et al. Orchestration of the DNA-damage response by the RNF8 ubiquitin ligase. *Science*. 2007; 318:1637–1640.10.1126/science.1150034 [PubMed: 18006705]
38. Rogakou EP, Boon C, Redon C, Bonner WM. Megabase chromatin domains involved in DNA double-strand breaks in vivo. *J Cell Biol*. 1999; 146:905–916. [PubMed: 10477747]
39. Cotsiki M, et al. Simian virus 40 large T antigen targets the spindle assembly checkpoint protein Bub1. *Proceedings of the National Academy of Sciences of the United States of America*. 2004; 101:947–952.10.1073/pnas.0308006100 [PubMed: 14732683]
40. Murray JM, Stiff T, Jeggo PA. DNA double-strand break repair within heterochromatic regions. *Biochemical Society transactions*. 2012; 40:173–178.10.1042/BST20110631 [PubMed: 22260685]

41. Hammet A, Magill C, Heierhorst J, Jackson SP. Rad9 BRCT domain interaction with phosphorylated H2AX regulates the G1 checkpoint in budding yeast. *EMBO reports*. 2007; 8:851–857.10.1038/sj.embor.7401036 [PubMed: 17721446]
42. Nakamura TM, Du LL, Redon C, Russell P. Histone H2A phosphorylation controls Crb2 recruitment at DNA breaks, maintains checkpoint arrest, and influences DNA repair in fission yeast. *Molecular and cellular biology*. 2004; 24:6215–6230.10.1128/MCB.24.14.6215-6230.2004 [PubMed: 15226425]
43. Sanders SL, Arida AR, Phan FP. Requirement for the phospho-H2AX binding module of Crb2 in double-strand break targeting and checkpoint activation. *Molecular and cellular biology*. 2010; 30:4722–4731.10.1128/MCB.00404-10 [PubMed: 20679488]
44. Bothmer A, et al. Regulation of DNA end joining, resection, and immunoglobulin class switch recombination by 53BP1. *Mol Cell*. 2011; 42:319–329. [PubMed: 21549309]
45. Callen E, et al. 53BP1 mediates productive and mutagenic DNA repair through distinct phosphoprotein interactions. *Cell*. 2013; 153:1266–1280.10.1016/j.cell.2013.05.023 [PubMed: 23727112]
46. Ward I, et al. The tandem BRCT domain of 53BP1 is not required for its repair function. *J Biol Chem*. 2006; 281:38472–38477. [PubMed: 17043355]
47. Cann KL, Dellaire G. Heterochromatin and the DNA damage response: the need to relax. *Biochemistry and cell biology = Biochimie et biologie cellulaire*. 2011; 89:45–60.10.1139/O10-113 [PubMed: 21326362]
48. Noon AT, et al. 53BP1-dependent robust localized KAP-1 phosphorylation is essential for heterochromatic DNA double-strand break repair. *Nature cell biology*. 2010; 12:177–184.10.1038/ncb2017 [PubMed: 20081839]
49. Schoeftner S, Blasco MA. A ‘higher order’ of telomere regulation: telomere heterochromatin and telomeric RNAs. *The EMBO journal*. 2009; 28:2323–2336.10.1038/emboj.2009.197 [PubMed: 19629032]
50. Ruthenburg AJ, Li H, Patel DJ, Allis CD. Multivalent engagement of chromatin modifications by linked binding modules. *Nature reviews. Molecular cell biology*. 2007; 8:983–994.10.1038/nrm2298 [PubMed: 18037899]
51. Cox J, Mann M. MaxQuant enables high peptide identification rates, individualized p.p.b.-range mass accuracies and proteome-wide protein quantification. *Nature biotechnology*. 2008; 26:1367–1372.10.1038/nbt.1511



**Figure 1.** Chemical probes to capture direct  $\gamma$ H2AX interaction partners. **(a)** Chemical structures of probe C, probe 1 and probe 2. **(b)** A strategy for capturing direct 'readers' of  $\gamma$ H2AX. **(c)** Dose-dependent cross-linking of probe 1 or probe 2 to MDC1-BRCT. Purified MDC1-BRCT was mixed with various concentrations of probe and exposed to 365 nm UV light. Cross-linked complexes were detected by Western blot using streptavidin-based detection (see Supplementary Fig. 10 for full blot). **(d)** Photo-cross-linking between probe 1 and MDC1-BRCT in the presence of a  $\gamma$ H2AX peptide (Ac-KKATQApSQEY-OH). Reactions containing probe 1 (1  $\mu$ M), MDC1-BRCT (200 nM), and various concentrations of  $\gamma$ H2AX peptide were performed and analyzed as described in **(c)** (see Supplementary Fig. 10 for full blot). **(e)** Quantification of cross-linking between MDC1-BRCT and probe 1 in the presence of  $\gamma$ H2AX or H2AX (Ac-KKATQASQEY-OH) competitor peptides (Supplementary Fig. 2). Cross-linked species were quantified by densitometry and values were fit to a single-site binding model to calculate an  $IC_{50}$ . Data represent mean values  $\pm$  s. d. (n=3).

**Figure 2.**

Proteomic profiling of high-affinity direct binders of  $\gamma$ H2AX. **(a)** Schematic for the identification of cellular proteins whose photo-cross-linking to probe 1 is inhibited by the presence of soluble  $\gamma$ H2AX peptide (Ac-KKATQApSQEY-OH). Isotopically labeled lysate generated from nocodazole-arrested HeLa cells was photo-cross-linked with probe 1 (5  $\mu$ M) or probe 1 (5  $\mu$ M) supplemented with  $\gamma$ H2AX peptide (50  $\mu$ M). After photo-cross-linking, samples were combined and subjected to streptavidin affinity pull-down. Following elution from beads, proteins were separated by SDS-PAGE and digested in-gel with trypsin. LC-MS/MS analysis was then used to identify and quantify isotopically matched peptide pairs. **(b)** Plot of protein enrichment ratios (expressed as  $\log_2$ ) from 'forward' and 'reverse' labeling experiments. Proteins exhibiting reproducible enrichment ratios  $>1.5$  are indicated. **(c)** MS1 spectra for an isotopically matched peptide pair for 'forward' and 'reverse' experiments corresponding to the protein MDC1. **(d)** Western blot analysis of 53BP1 photo-cross-linking to probe 1 in HeLa cell lysate. Lysate from nocodazole-treated or untreated

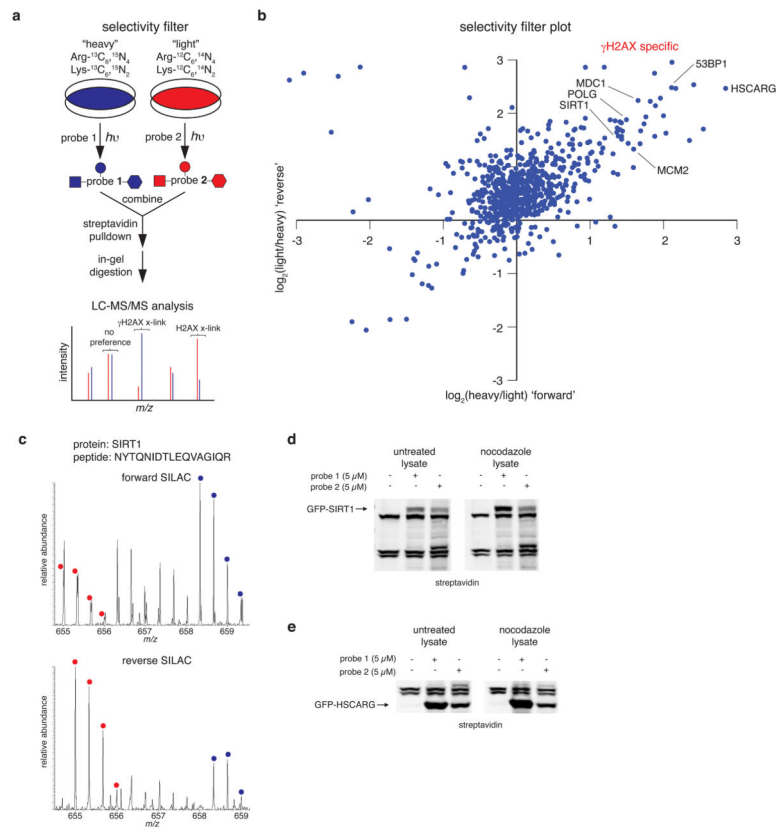
HeLa cells was photo-cross-linked in the presence of probe 1 (5  $\mu\text{M}$ ) or probe 1 (5  $\mu\text{M}$ ) supplemented with  $\gamma\text{H2AX}$  peptide (50  $\mu\text{M}$ ). Streptavidin enrichment followed by Western blot with an anti-53BP1 antibody was performed. DM1 $\alpha$  (anti  $\alpha$ -tubulin) antibody was used to verify equal protein concentration. Data is representative of 2 independent experiments (see Supplementary Fig. 10 for full blot).

Author Manuscript

Author Manuscript

Author Manuscript

Author Manuscript

**Figure 3.**

Proteomic profiling of phospho-selective direct binders of  $\gamma$ H2AX. **(a)** Schematic for the identification of cellular proteins preferentially photo-cross-linking to probe 1 relative to probe 2 (i.e. 'selectivity filter'). SILAC-labeled lysate generated from nocodazole-arrested HeLa cells was photo-cross-linked with probe 1 or probe 2 (5  $\mu$ M), combined, and subjected to streptavidin affinity pull-down. Following elution from beads, proteins were separated by SDS-PAGE and digested in-gel with trypsin. LC-MS/MS analysis was then used to identify and quantify isotopically matched SILAC peptide pairs. **(b)** Plot of SILAC ratios (expressed as log<sub>2</sub>) from 'forward' and 'reverse' 'selectivity filter' experiments. Known chromatin-binding proteins exhibiting reproducible photo-cross-linking behavior in the 'forward' and 'reverse' runs are indicated. **(c)** MS1 spectra for a SILAC peptide pair from 'forward' and 'reverse' 'selectivity filter' experiments corresponding to the protein SIRT1. Red and blue circles identify isotope peaks for 'light' and 'heavy' peptides, respectively. **(d)** Phospho-selective photo-cross-linking of recombinant GFP-SIRT1. Lysate harvested from untreated or nocodazole-arrested HEK293T cells transiently expressing GFP-SIRT1 was UV irradiated in the presence of probe 1, probe 2, or no probe. After photo-cross-linking, Western blot with streptavidin-based detection was used to identify cellular proteins that reacted with the respective probes. The arrow indicates the band corresponding to GFP-SIRT1 as confirmed by anti-GFP Western blot. Data is representative of 3 independent experiments (see Supplementary Fig. 10 for full blot). **(e)** Phospho-selective photo-cross-linking of recombinant GFP-HSCARG. Reactions were performed and analyzed as described in **(d)** (see Supplementary Fig. 10 for full blot).



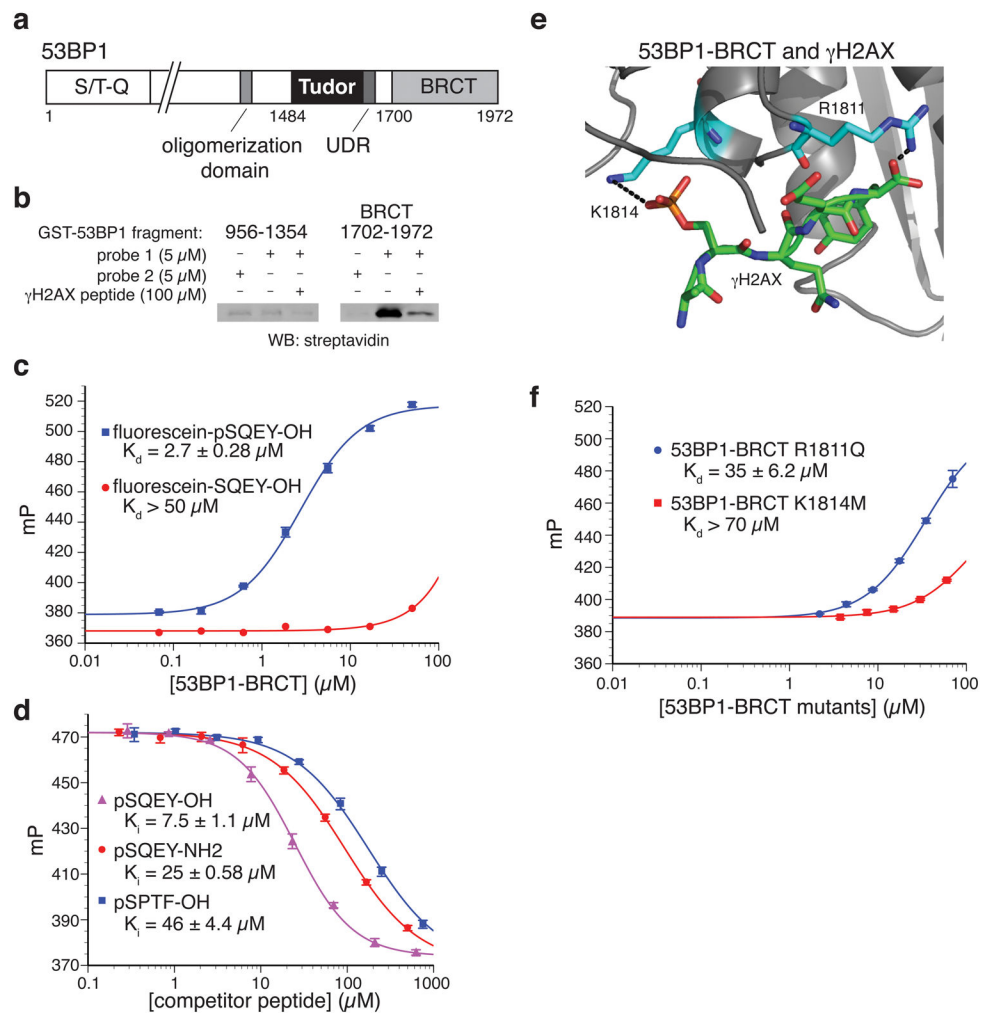


**Figure 4.** Biochemical characterization of the 53BP1- $\gamma$ H2AX interaction. **(a)** Domain structure of 53BP1. Motifs involved in recruitment to  $\gamma$ H2AX foci—the oligomerization domain, tandem Tudor domains, and UDR motif—are found in the C-terminal portion of the protein. **(b)** Photo-cross-linking of probes 1 and 2 to recombinant GST-tagged fragments of 53BP1. Proteins corresponding to residues 956-1354 or 1702-1972 were photo-cross-linked in the presence of probe 1 (5  $\mu$ M), probe 2 (5  $\mu$ M), or probe 1 (5  $\mu$ M) with  $\gamma$ H2AX peptide (100  $\mu$ M). Western blot with streptavidin-based detection was used to analyze the extent of photo-cross-linking to the probe. Data are representative of 2 independent experiments (see Supplementary Fig. 10 for full blot). **(c)** Characterization of binding between 53BP1-BRCT and fluorescein-pSQEY-OH or fluorescein-SQEY-OH peptides using fluorescence anisotropy. Data represent the mean  $\pm$  s.d. (n=3). **(d)** Characterization of competitive binding between fluorescein-pSQEY-OH and unlabeled tetrapeptides for 53BP1-BRCT using fluorescence anisotropy. Data represent the mean  $\pm$  s.d. (n=3). **(e)** A structural model of 53BP1-BRCT binding to a  $\gamma$ H2AX peptide. The structures of 53BP1-BRCT (pdb: 1KZY) and MDC1-BRCT: $\gamma$ H2AX (pdb: 2AZM) were aligned using PyMol. Putative interactions between conserved 53BP1-BRCT residues (teal) and  $\gamma$ H2AX (green) are shown with dotted

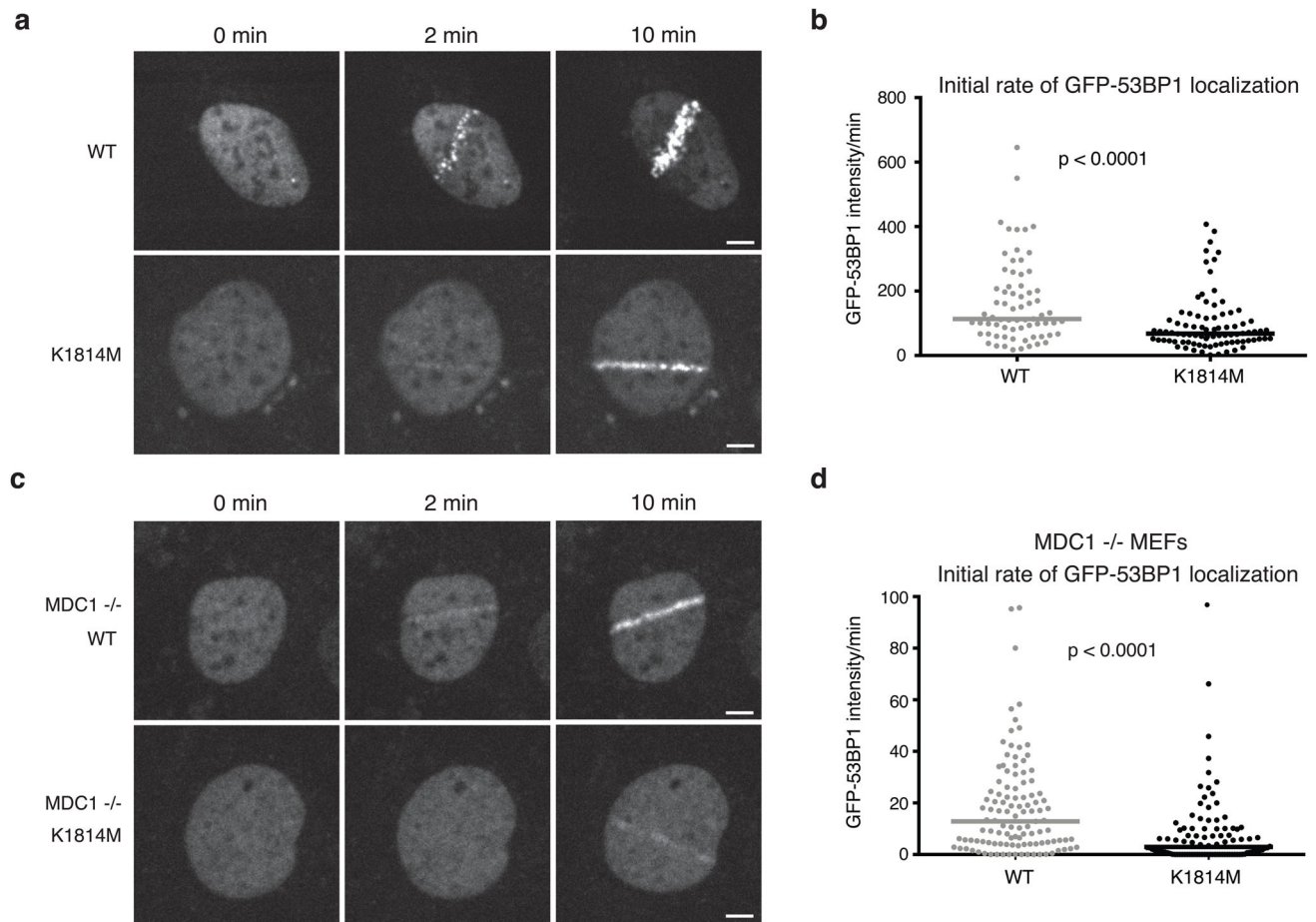
black lines. **(f)** Characterization of binding between mutant 53BP1-BRCT proteins and fluorescein-pSQEY-OH using fluorescence anisotropy. Data represent the mean  $\pm$  s.d. (n=3).

Author Manuscript

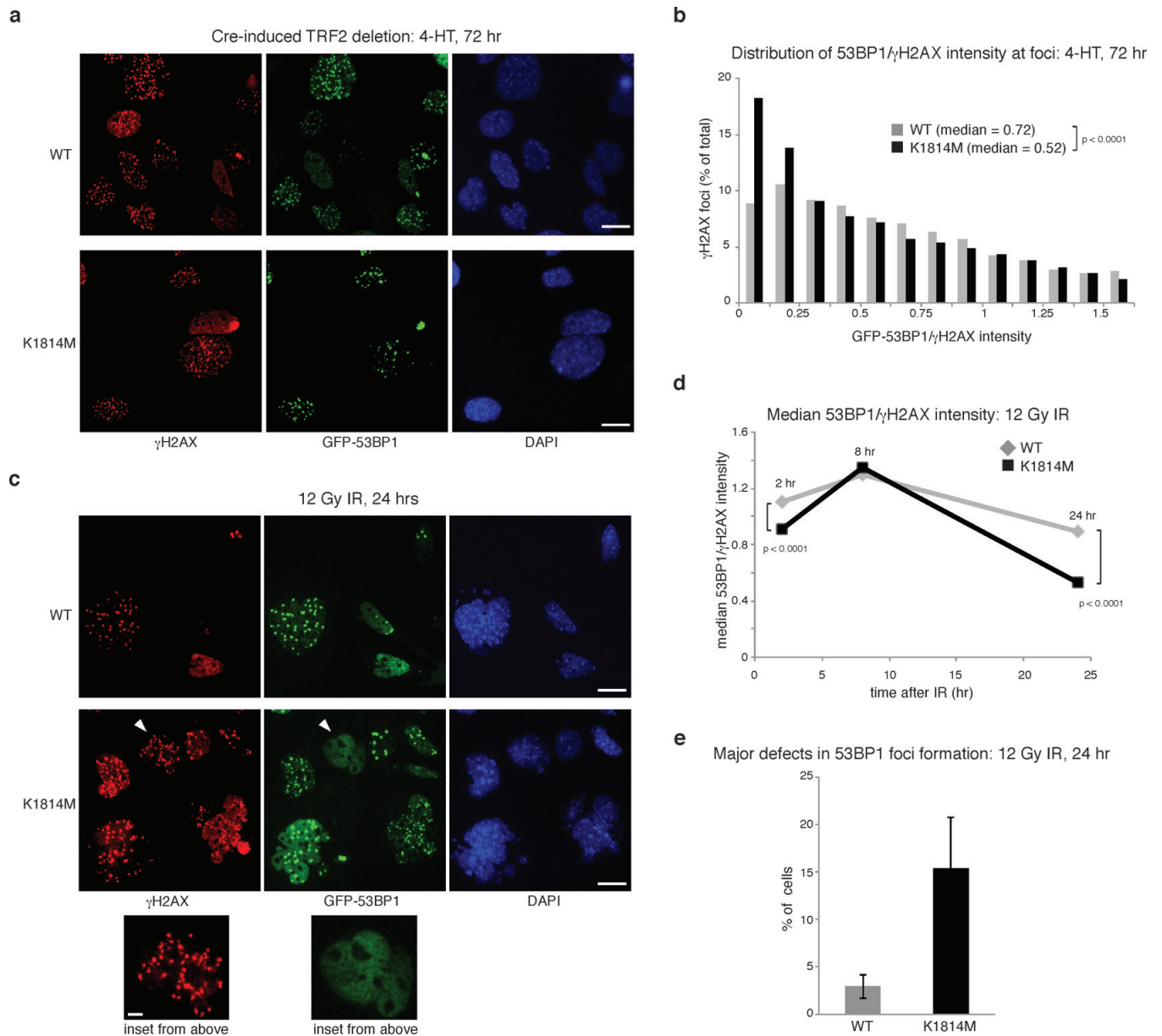
Author Manuscript

Author Manuscript

Author Manuscript

**Figure 5.**

Live-cell analysis of 53BP1 localization at DNA damage produced by ‘laser scissors’. **(a)** 53BP1<sup>-/-</sup>TRF2<sup>F/-</sup> MEFs expressing WT or K1814M GFP-53BP1 were exposed to 405 nm laser light in a stripe pattern and GFP-53BP1 localization was monitored by confocal microscopy over 10 min (4 min, 6 min and 8 min time points can be found in Supplementary Fig. 5). Scale bar is 5  $\mu$ m. **(b)** Quantification of the initial rate of 53BP1 accumulation in WT and K1814M 53BP1-expressing cells after laser damage. The change in fluorescence intensity was measured in the first 4 min of recruitment and fit by linear regression analysis. The solid line corresponds to the median of all data points (n = 69 WT cells, 86 K1814M cells; 3 independent experiments; significance between median values was analyzed using the two-tailed Mann-Whitney test). **(c)** MDC1<sup>-/-</sup> MEFs expressing WT or K1814M GFP-53BP1 were exposed to 405 nm laser light in a stripe pattern and GFP-53BP1 localization was monitored by confocal microscopy over 10 min (4 min, 6 min and 8 min time points can be found in Supplementary Fig. 5). Scale bar is 5  $\mu$ m **(d)** Quantification of the initial rate of 53BP1 accumulation in MDC1<sup>-/-</sup> MEFs. The change in fluorescence intensity was measured between 2 min and 10 min following laser-induced damage and fit by linear regression analysis. Data was analyzed and plotted as in **(b)** (n = 113 WT cells, 98 K1814M cells; 3 independent experiments).

**Figure 6.**

Comparative analysis of WT and K1814M 53BP1 and  $\gamma$ H2AX foci generated in response to TRF2 depletion or IR. **(a)** Immunofluorescence analysis of 53BP1<sup>-/-</sup>TRF2<sup>F/-</sup> MEFs expressing WT or K1814M GFP-53BP1 72 hr after treatment with 4-HT. Cells were stained with anti- $\gamma$ H2AX (red), anti-GFP (green), and DAPI (blue). Scale bar is 20  $\mu$ m **(b)** Quantification of 53BP1 accumulation at  $\gamma$ H2AX foci 72 hr after 4-HT treatment. 53BP1/ $\gamma$ H2AX intensity was measured for all identified foci (n = 6985 WT foci, 7329 K1814M foci; 3 independent experiments). Bins containing > 2.5% of total foci are shown (full distribution can be found in Supplementary Fig. 6). Significance between median 53BP1/ $\gamma$ H2AX intensity values was analyzed using the two-tailed Mann-Whitney test. **(c)** Immunofluorescence analysis of 53BP1<sup>-/-</sup>TRF2<sup>F/-</sup> MEFs expressing WT or K1814M GFP-53BP1 24 hr after 12 Gy IR. White arrows indicate cells exhibiting gross defects in

53BP1 localization at  $\gamma$ H2AX foci. Scale bar is 20  $\mu$ m (5  $\mu$ m in inset). **(d)** Median 53BP1/ $\gamma$ H2AX intensity over all  $\gamma$ H2AX foci during the course of the response to 12 Gy IR. Cells were analyzed 2 hr (n=11596 WT foci, 11616 K1814M foci; 3 independent experiments) 8 hr (n=7225 WT foci, 10196 K1814M foci; 3 independent experiments), and 24 hr (n=3917 WT foci, 4768 K1814M foci; 3 independent experiments) following IR treatment. **(e)** Quantification of cells exhibiting major defects (>90% of  $\gamma$ H2AX foci lack co-localizing 53BP1 foci) in 53BP1 localization at  $\gamma$ H2AX foci, measured 24 hr after 12 Gy. Values represent mean  $\pm$  s.d. (n>50 cells per experiment; 3 independent experiments).